Electronic Supplementary Material (ESI) for Journal of Materials Chemistry A.

Supplementary Information

Lateral built-in field of 2D/2D SnS_2/$SnSe_2$ in-plane heterostructure with boosted interfacial charge transfer

Ruozhen Wu[a], Tiezhu Xin[a], You Wang[a], Tingting Wang[a], Lizhao Liu[b]* and Juanyuan Hao[a]**

[a]School of Materials Science and Engineering, Harbin Institute of Technology, Harbin 150001, P. R. China.

[b]Key Laboratory of Materials Modification by Laser, Ion and Electron Beams (Ministry of Education), School of Physics, Dalian University of Technology, Dalian 116024, PR China

*Corresponding authors.

E-mail addresses: jyhao@hit.edu.cn (J. Hao), lizhao_liu@dlut.edu.cn (L. Liu), y-wang@hit.edu.cn (Y. Wang)

DFT calculation results:

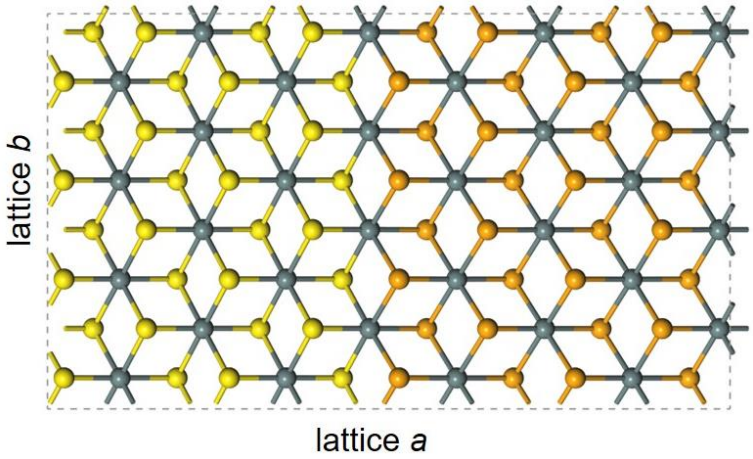

Fig. S1. The slab model of $Sn_{32}S_{32}Se_{32}$ supercell for $SnS_2/SnSe_2$ lateral heterojunction, where the lateral heterojunction is a= 26.17 Å / b=15.13 Å. The orange, yellow, and grey balls are Se, S, and Sn atoms, respectively.

Table S1. Bandgap values derived from the density of states (DOS) in different domains of $SnS_2/SnSe_2$ lateral heterojunction.

Domains	SnS_2	Heterointerface	$SnSe_2$
Bandgap (E_g)	0.83	**0.41**	0.44

Analyzed results of DFT calculations. The adsorption energis (E_{ads}) for NO_2 molecule on the surface of $SnS_2/SnSe_2$ lateral slab shows that the E_{ads} value of interface domain is more negative than that of SnS_2 and $SnSe_2$ domains (**Fig. 1a**), which the negative value represents the exothermic process, indicating the interfaces could serve as the active sites for NO_2 adsorption. Moreover, the charge density difference of the lateral heterojunctions shows the efficient diffusion of charge carriers across interface (**Fig. 1b**), which originates from the transport bridge of chemical bond S-Sn-Se and is conducive to improving the charge separation and transfer kinetics. The reduced bandgap of the interface domian (**Fig. 1c** and **Table S1**) indicates the improved electrical conductivity in $SnS_2/SnSe_2$ lateral heterostructure which could serve as a channel to boost charge transfer along the 2D basal plane to react with electrophilic NO_2 molecules, contributing to enhancing the gas sensing performance. The DOS of interface in the valence band near the Fermi level shows that the holes in the valence band are mainly contributed by Se (**Fig. 1c**), implying that the electrons of $SnSe_2$ near the interface tend to diffuse into SnS_2 while leaving holes in $SnSe_2$.

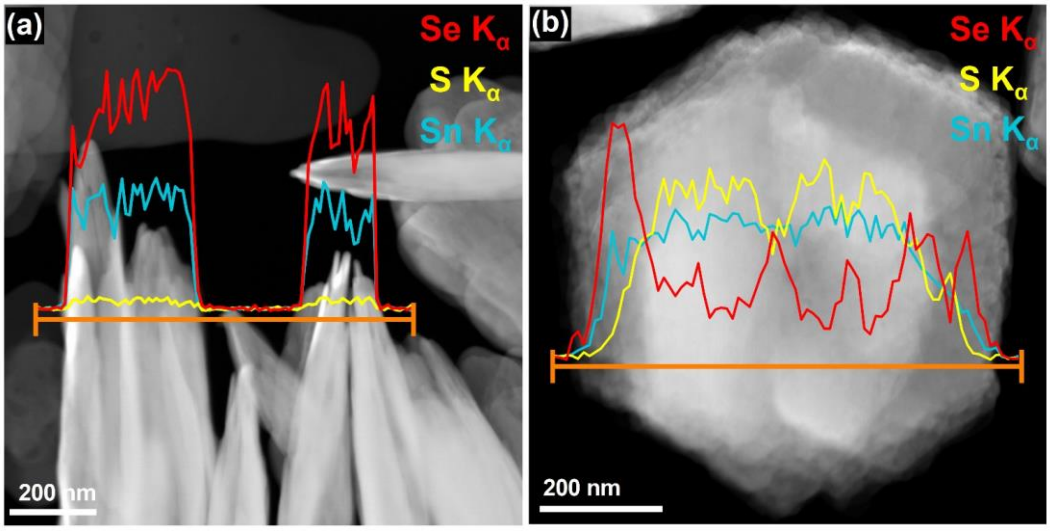

Fig. S2. HAADF-STEM image of $SnS_2/SnSe_2$-2 nanosheets, with composition determined from the EDX profile along orange line of Se Kα (red line), S Kα (yellow line) and Sn Kα (cyan line) signals: (a) side view, (b) top view. The results show that the spatial distribution of Se and S elements have the highest and lowest concentration at the edges, respectively, indicating that the *in-situ* grown $SnSe_2$ interfaces with the SnS_2 to form a lateral rather than vertical 2D/2D heterostructure at low concentration of Se precursor.

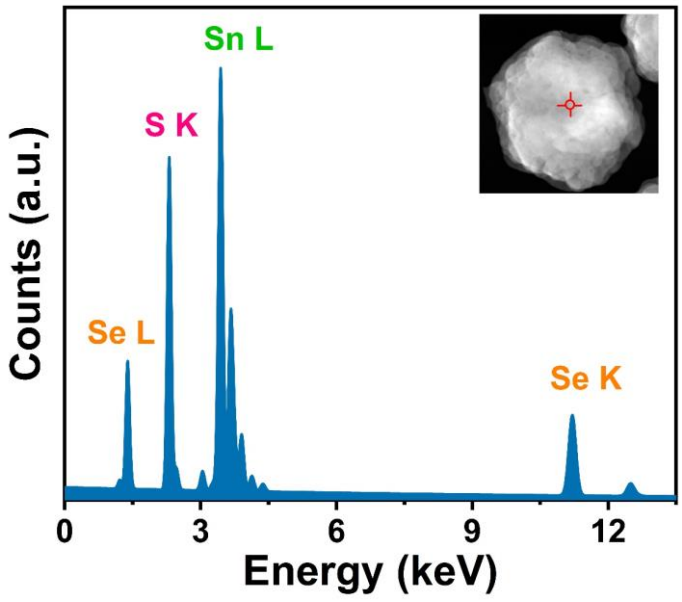

Fig. S3. EDX spot analysis in the core region of $SnS_2/SnSe_2$-3 nanosheet. The result shows the coexistence of Se and S elements in the core region of $SnS_2/SnSe_2$-3, further confirming the formation of the core-shell heterostructure for $SnS_2/SnSe_2$-3.

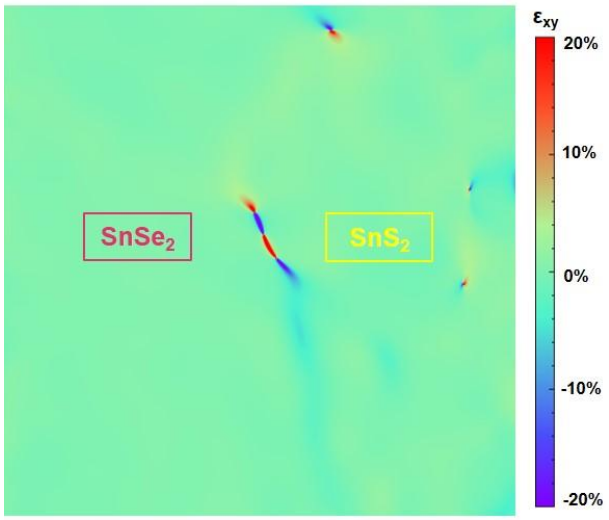

Fig. S4. geometric phase analysis (GPA) map deriving from the HRTEM image of $SnS_2/SnSe_2$-2 heterostructure. The result indicates the low density of stacking faults between the parent SnS_2 and derived $SnSe_2$, confirming the formation of sharp lattice-matched heterointerface.

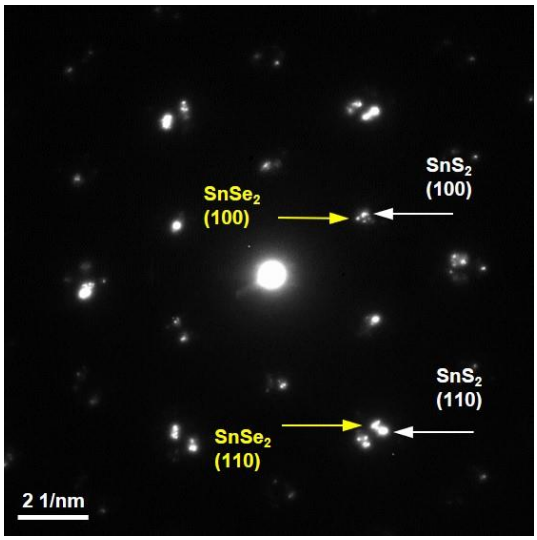

Fig. S5. SAED pattern of $SnS_2/SnSe_2$-2 heterostructure. The result shows an approximate hexagon in distribution with two identifiable groups of diffraction spots in the same orientation, corresponding to the $SnSe_2$ and SnS_2, respectively.

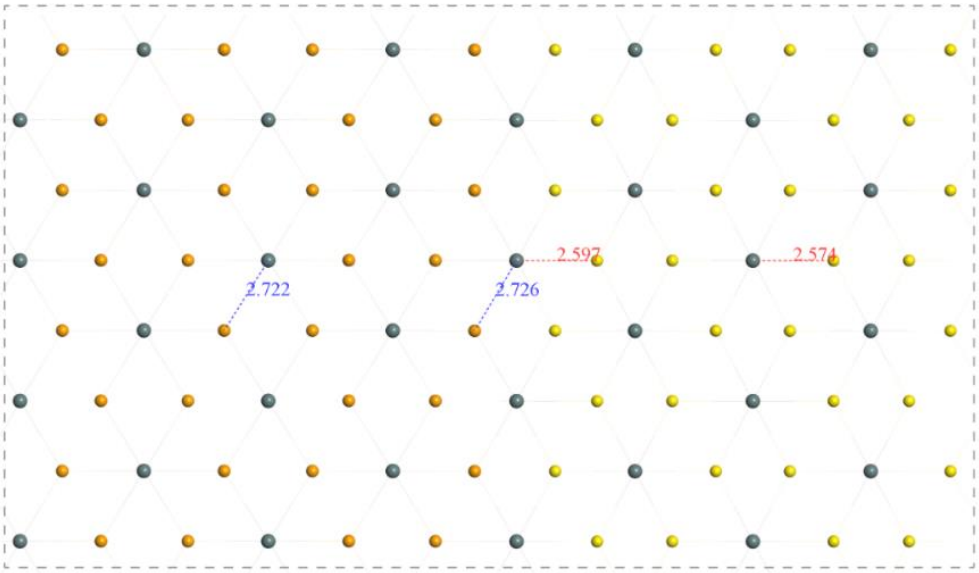

Fig. S6. Atomic arrangement and bond lengths of Se-Sn and S-Sn bonds in $SnSe_2$ region, interface, and SnS_2 region of 2D $SnS_2/SnSe_2$ lateral heterostructure. The orange, yellow, and grey balls represent the Se, S, and Sn atoms, respectively.

Table S2. The bond lengths and bond orders around the interface of $SnS_2/SnSe_2$ lateral heterostructure. The number after the element is the serial number of the element in the $SnS_2/SnSe_2$ lateral heterostructure.

	Bond Length (Å)	Bond Order
S7-Sn22	2.574	0.39
S18-Sn24-Se29	2.597, 2.726	0.35, 0.03
Se12-Sn6	2.722	0.20

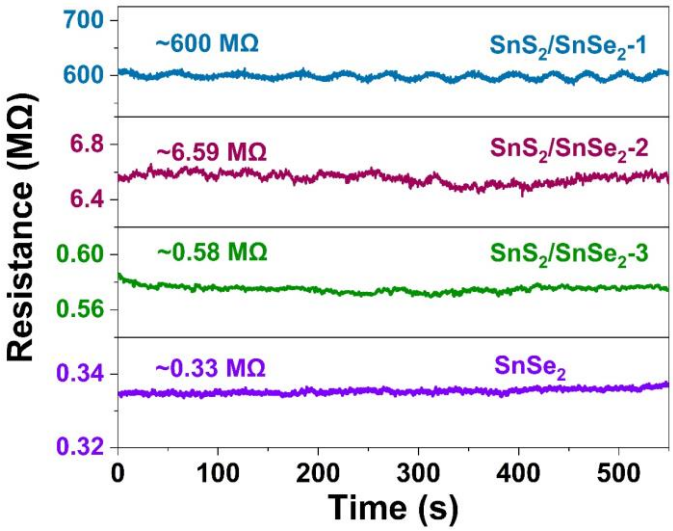

Fig. S7. Baseline resistance of SnS_2 template, $SnS_2/SnSe_2$-1, $SnS_2/SnSe_2$-2, $SnS_2/SnSe_2$-3, and $SnSe_2$. The baseline resistance sharply declines after the formation of $SnS_2/SnSe_2$ heterostructure, from ~600 MΩ of $SnS_2/SnSe_2$-1 to ~0.58 MΩ of $SnS_2/SnSe_2$-3 that is close to ~0.33 MΩ of $SnSe_2$, indicating that the formation of 2D/2D seamless stitching $SnS_2/SnSe_2$ heterostructure significantly modulates the electronic structure and improves the conductivity of SnS_2. This is due to that the electrons of $SnSe_2$ diffuse into the SnS_2 to increase the electron density of SnS_2, contributing to the lower resistance of heterostructure than that of pristine SnS_2.

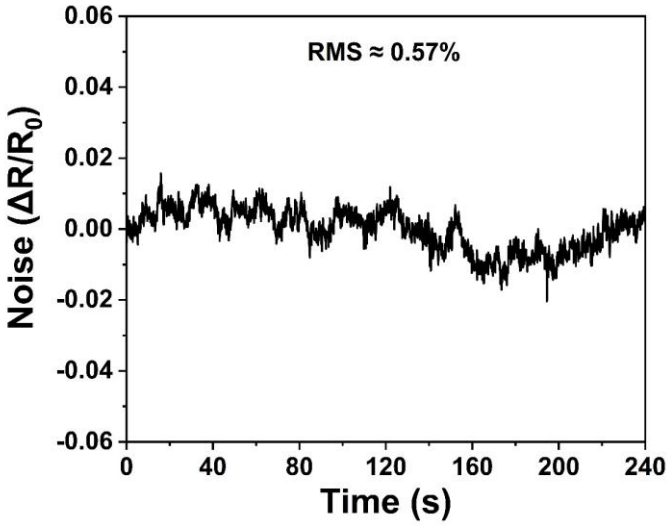

Fig. S8. Experimentally recorded noise of response for the $SnS_2/SnSe_2$-2 sensor. The result indicates that the root-mean-square (RMS) value of background noise is about 0.57%.

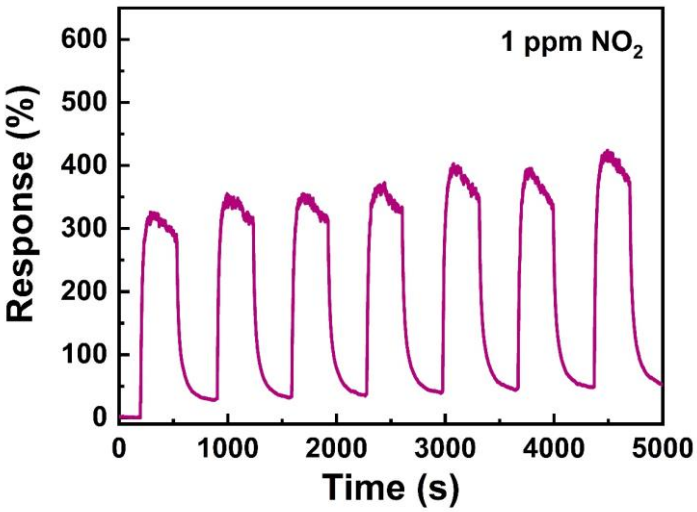

Fig. S9. Repeatability test of $SnS_2/SnSe_2$-2 conducted by seven successive cycles upon the exposure of 1 ppm NO_2 at room temperature. The result shows the good reversible response and recovery with the nearly same response value.

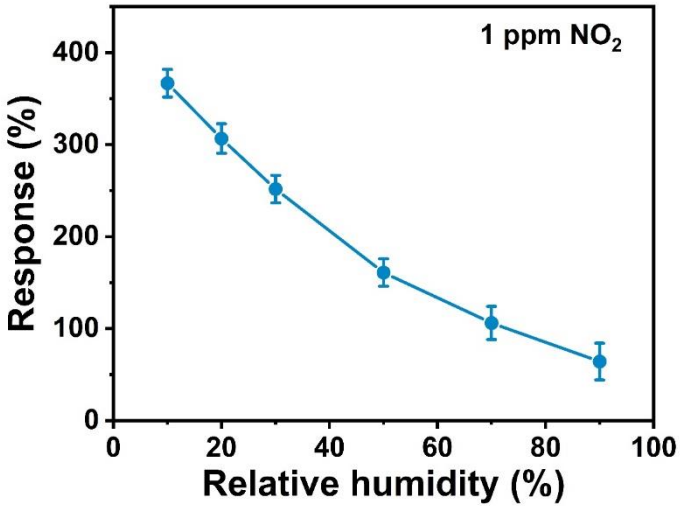

Fig. S10. Evolution of response with the relative humidity increasing from 10% to 90% for $SnS_2/SnSe_2$-2. The result shows that the response of $SnS_2/SnSe_2$-2 decreases with the relative humidity changing from 10% to 90%, which may be ascribe to the strong competitive adsorption between H_2O and NO_2 molecules.

Table S3. The sensing properties of $SnS_2/SnSe_2$-2 sensor compared with the state-of-the-art resistive-type SnS_2-based NO_2 sensors in literature.

t_{res} = Response time, t_{rec} = Recovery time, RT* = Light illumination at room temperature.

Sensing materials	Condition (°C)	NO_2 (ppm)	Response (%)	t_{res}/t_{rec} (s/s)	Sensitivity (% ppm^{-1})	Detection Limit (ppb)	Reference
SnS_2 flakes	150	10	2000	- / -	~570	300	[1]
2D SnS_2/rGO	150	5	3200	50 / 48	/	500	[2]
Mo-doped SnS_2	150	100	4751	33.5 / 21	/	/	[3]
3D SnS_2/rGO	RT	8	49.8	153 / 76	6.1	8.7	[4]
SnS_2/MoS_2	RT	5	270	2.9 / 24.5	/	50	[5]
SnS_2/SnS	RT	4	660	365 / 1216	~200	75	[6]
S-rich SnS_2	RT	10	701	272 / 3800	0.5	1000	[7]
SnS_2 flowers	RT*	5	1428	400 / 1100	251	400	[8]
$SnSe_2$/SnSe	RT*	1	~600	- / >300	6.1	100	[9]
$SnS_2/SnSe_2$-2	**RT**	**4**	**1165.2**	**80 / 78**	**322.0**	**50**	**This work**

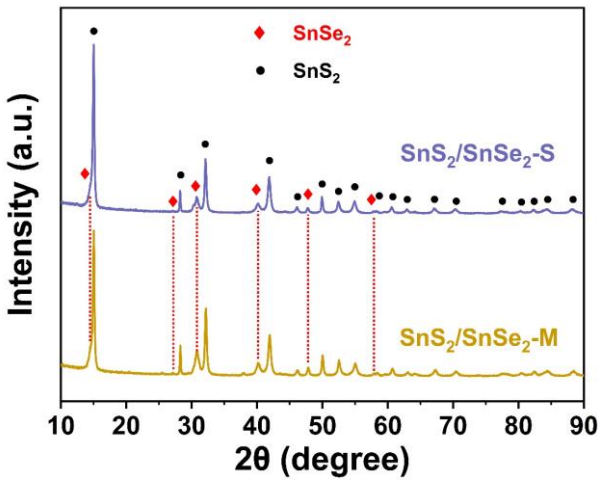

Fig. S11. XRD patterns of $SnS_2/SnSe_2$-M and $SnS_2/SnSe_2$-S heterostructures. The $SnS_2/SnSe_2$-M and $SnS_2/SnSe_2$-S heterostructures were synthesized by physical mixing and solvothermal deposition approaches, respectively. The XRD results show the coexistence of SnS_2 and $SnSe_2$ crystals without any other impurities, indicating the formation of $SnS_2/SnSe_2$-M and $SnS_2/SnSe_2$-S heterostructures.

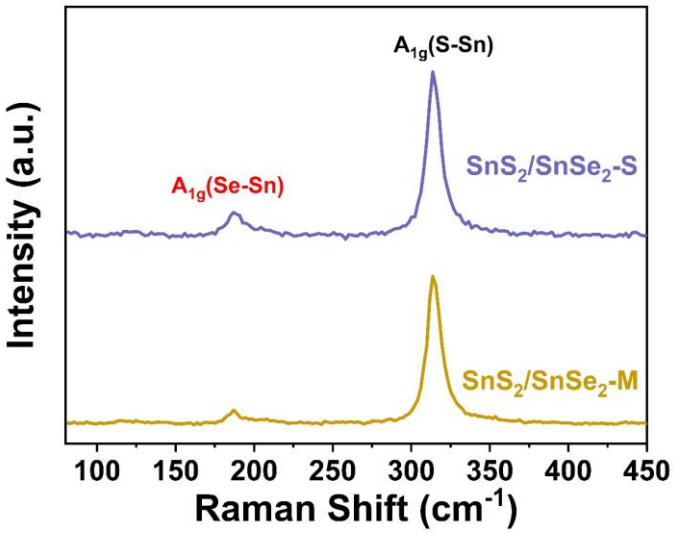

Fig. S12. Raman spectra of $SnS_2/SnSe_2$-M and $SnS_2/SnSe_2$-S heterostructures. The results show the vibration modes of layered SnS_2 and $SnSe_2$ crystals, which is consistent with the XRD result, verifying that the formation of $SnS_2/SnSe_2$-M and $SnS_2/SnSe_2$-S heterostructures.

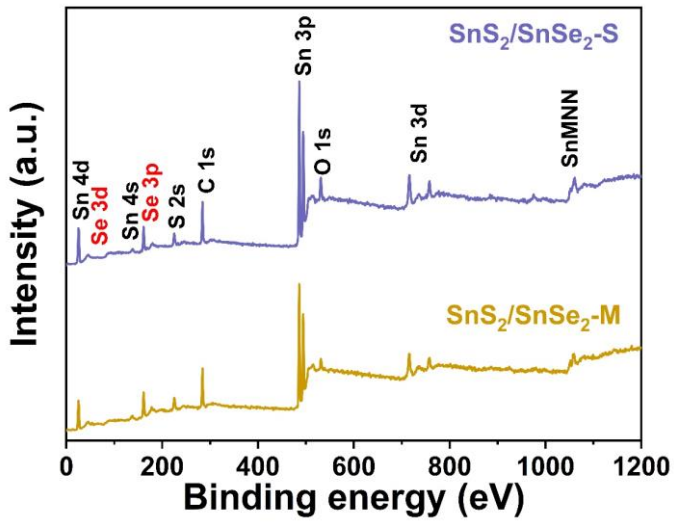

Fig. S13. XPS elemental survey spectra of $SnS_2/SnSe_2$-M and $SnS_2/SnSe_2$-S heterostructures. The results show the coexistence of S and Se elements without impurities in the $SnS_2/SnSe_2$-M and $SnS_2/SnSe_2$-S heterostructures, confirming that the formation of $SnS_2/SnSe_2$-M and $SnS_2/SnSe_2$-S heterostructures.

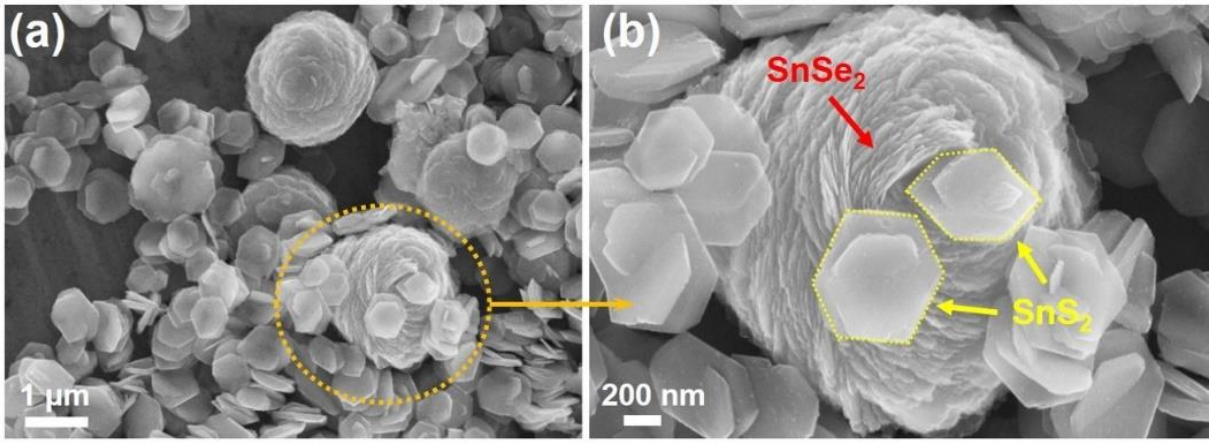

Fig. S14. SEM images of $SnS_2/SnSe_2$-M heterostructure. The SEM images of $SnS_2/SnSe_2$-M display that the hexagonal SnS_2 crystals (marked by yellow) randomly and loosely stack on the $SnSe_2$ crystals (marked by red), indicating a poor-quality heterointerface of $SnS_2/SnSe_2$-M.

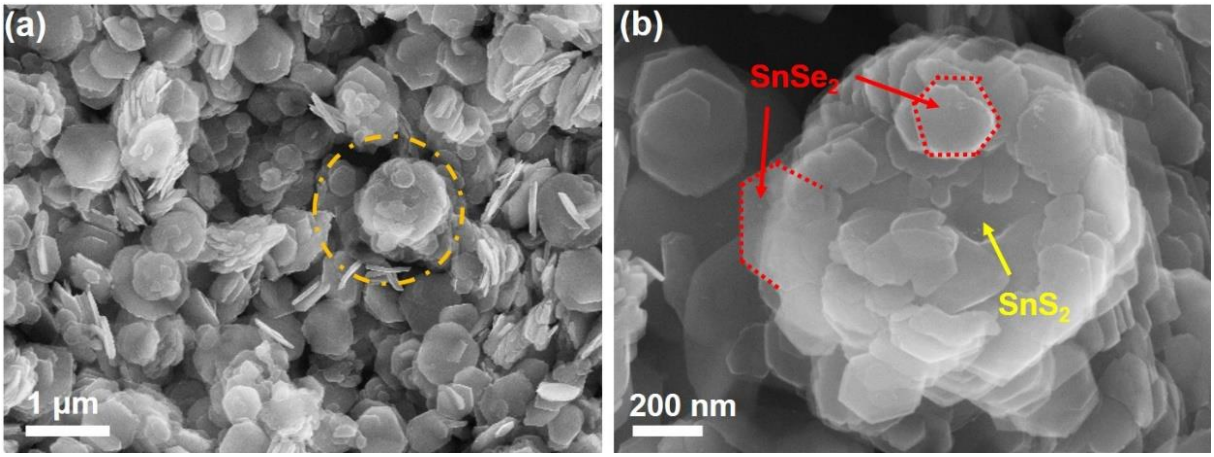

Fig. S15. SEM images of $SnS_2/SnSe_2$-S heterostructure. The SEM images of $SnS_2/SnSe_2$-S show that the $SnSe_2$ crystals (marked by red) grow on the surface of SnS_2 nanosheets (marked by yellow) with a relatively intimate contact compared to the $SnS_2/SnSe_2$-M.

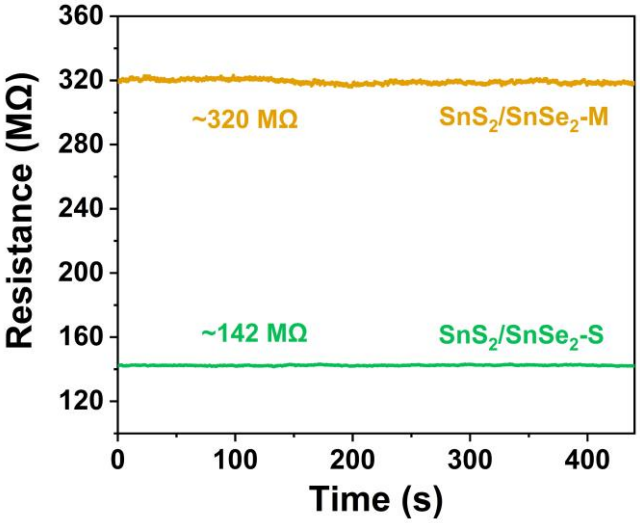

Fig. S16. The initial resistance of the sensors based on the $SnS_2/SnSe_2$-M and $SnS_2/SnSe_2$-S heterostructures. The smaller resistance of $SnS_2/SnSe_2$-S sensor may be due to the better contact and uniform dispersion between SnS_2 and $SnSe_2$, as compared with the $SnS_2/SnSe_2$-M.

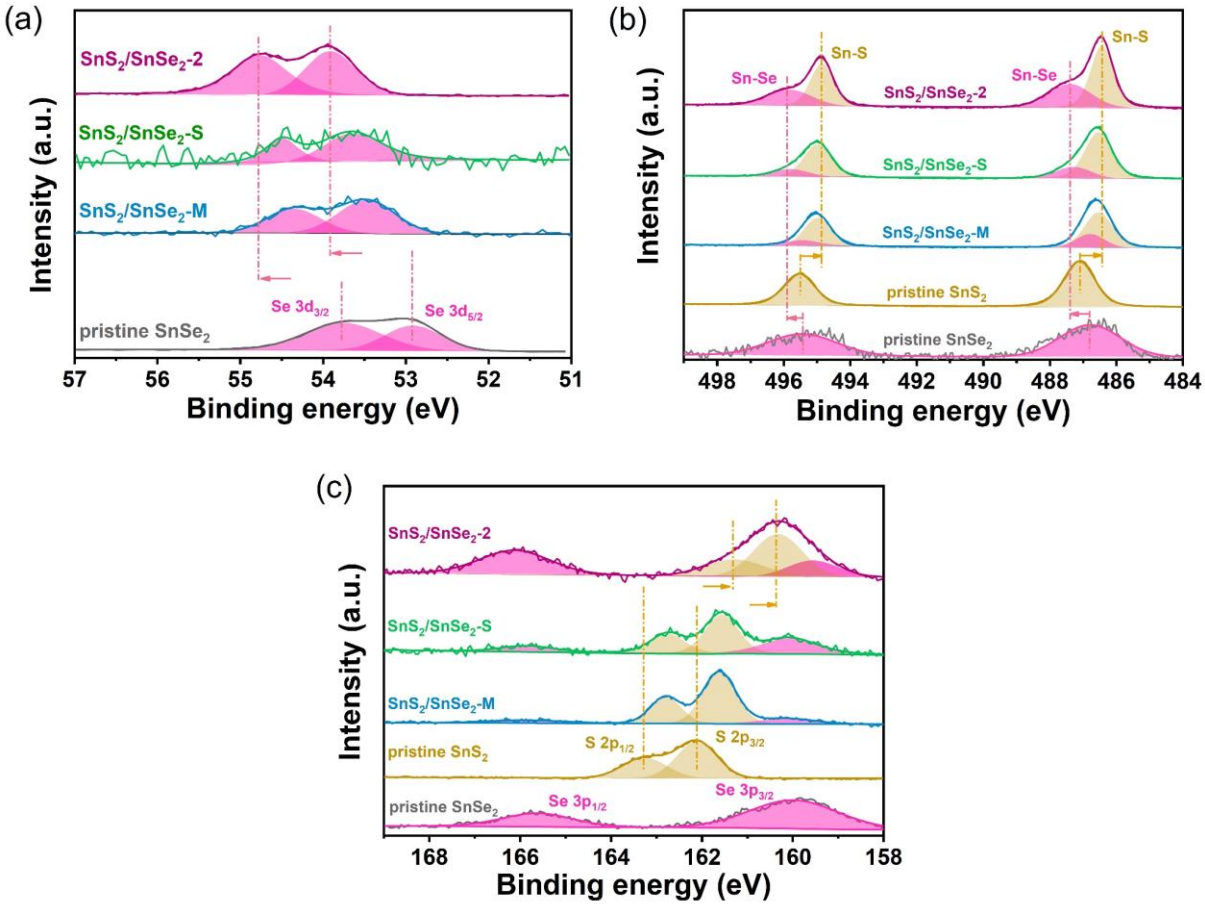

Fig. S17. High-resolution (a) Se 3d, (b) Sn 3d, and (c) S 2p & Se 3p XPS spectra for the pristine $SnSe_2$, pristine SnS_2, $SnS_2/SnSe_2$-M, $SnS_2/SnSe_2$-S, and $SnS_2/SnSe_2$-2.

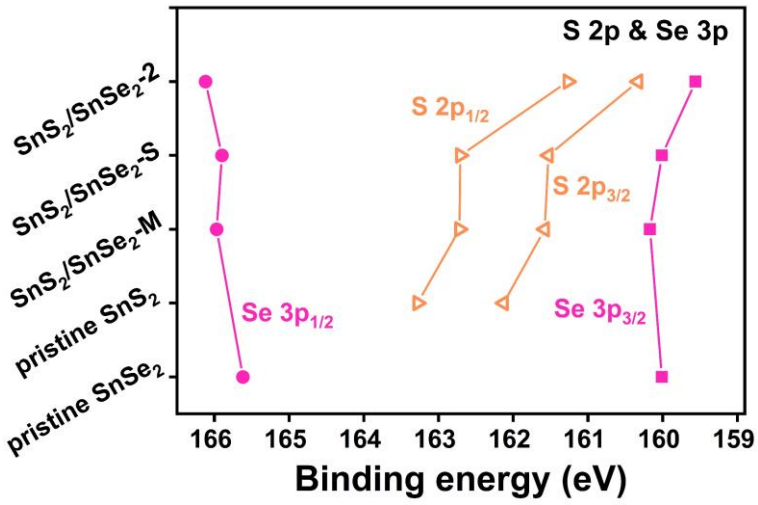

Fig. S18. The summarized S 2p and Se 3p peak positions for the pristine $SnSe_2$, pristine SnS_2, $SnS_2/SnSe_2$-M, $SnS_2/SnSe_2$-S, and $SnS_2/SnSe_2$-2 samples.

References:

[1] C. Kim, J. C. Park, S. Y. Choi, Y. Kim, S. Y. Seo, T. E. Park, S. H. Kwon, B. Cho, J. H. Ahn, *Small* **2018**, 14, 1704116.

[2] M. Cheng, Z. Wu, G. Liu, L. Zhao, Y. Gao, B. Zhang, F. Liu, X. Yan, X. Liang, P. Sun, G. Lu. *Sens. Actuato*r, B **2019**, 291, 216.

[3] J. Zhou, K. Xue, Y. Liu, T. Liang, P. Zhang, X. Zhang, W. Zhang, Z. Dai, *Chem. Eng. J.* **2021**, 420, 127572.

[4] J. Wu, Z. Wu, H. Ding, Y. Wei, W. Huang, X. Yang, Z. Li, L. Qiu, X. Wang, *Sens. Actuator*, B **2020**, 305, 127445.

[5] L. Liu, M. Ikram, L. Ma, X. Zhang, H. Lv, M. Ullah, M. Khan, H. Yu, K. Shi, *J. Hazard. Mater.* **2020**, 393, 122325.

[6] Q. Sun, J. Wang, J. Hao, S. Zheng, P. Wan, T. Wang, H. Fang, Y. Wang, *Nanoscale* **2019**, 11, 13741.

[7] K. C. Kwon, J. M. Suh, T. H. Lee, K. S. Choi, K. Hong, Y. G. Song, Y. S. Shim, M. Shokouhimehr, C. Y. Kang, S. Y. Kim, H. W. Jang, *ACS Sens.* **2019**, 4, 678.

[8] T. H. Eom, S. H. Cho, J. M. Suh, T. Kim, T. H. Lee, S. E. Jun, J. W. Yang, J. Lee, S.-H. Hong, H. W. Jang, *J. Mater. Chem.* A **2021**, 9, 11168.

[9] X. Wang, Y. Liu, J. Dai, Q. Chen, X. Huang, W. Huang, *Chem. Eur. J.* **2020**, 26, 3870.